JACS
JOURNAL OF THE AMERICAN CHEMICAL SOCIETY
Article
pubs.acs.org/JACS

Clathrate $Ba_8Au_{16}P_{30}$: The "Gold Standard" for Lattice Thermal Conductivity

James Fulmer,[†] Oleg I. Lebedev,[§] Vladimir V. Roddatis,[∥] Derrick C. Kaseman,[‡] Sabyasachi Sen,[‡] Juli-Anna Dolyniuk,[†] Kathleen Lee,[†] Andrei V. Olenev,[†] and Kirill Kovnir*[,†]

[†]Department of Chemistry and [‡]Department of Chemical Engineering and Materials Science, University of California, Davis, One Shields Avenue, Davis, California 95616, United States

[§]Laboratoire CRISMAT, ENSICAEN, CNRS UMR 6508, 6 Boulevard du Maréchal Juin, F-14050 Caen, France

[∥]CIC energiGUNE, Albert Einstein 48, 01510 Miñano, Álava, Spain

Supporting Information

ABSTRACT: A novel clathrate phase, $Ba_8Au_{16}P_{30}$, was synthesized from its elements. High-resolution powder X-ray diffraction and transmission electron microscopy were used to establish the crystal structure of the new compound. $Ba_8Au_{16}P_{30}$ crystallizes in an orthorhombic superstructure of clathrate-I featuring a complete separation of gold and phosphorus atoms over different crystallographic positions, similar to the Cu-containing analogue, $Ba_8Cu_{16}P_{30}$. Barium cations are trapped inside the large polyhedral cages of the gold−phosphorus tetrahedral framework. X-ray diffraction indicated that one out of 15 crystallographically independent phosphorus atoms appears to be three-coordinate. Probing the local structure and chemical bonding of phosphorus atoms with ^{31}P solid-state NMR spectroscopy confirmed the three-coordinate nature of one of the phosphorus atomic positions. High-resolution high-angle annular dark-field scanning transmission electron microscopy indicated that the clathrate $Ba_8Au_{16}P_{30}$ is well-ordered on the atomic scale, although numerous twinning and intergrowth defects as well as antiphase boundaries were detected. The presence of such defects results in the pseudo-body-centered-cubic diffraction patterns observed in single-crystal X-ray diffraction experiments. NMR and resistivity characterization of $Ba_8Au_{16}P_{30}$ indicated paramagnetic metallic properties with a room-temperature resistivity of 1.7 mΩ cm. $Ba_8Au_{16}P_{30}$ exhibits a low total thermal conductivity (0.62 W m^{-1} K^{-1}) and an unprecedentedly low lattice thermal conductivity (0.18 W m^{-1} K^{-1}) at room temperature. The values of the thermal conductivity for $Ba_8Au_{16}P_{30}$ are significantly lower than the typical values reported for solid crystalline compounds. We attribute such low thermal conductivity values to the presence of a large number of heavy atoms (Au) in the framework and the formation of multiple twinning interfaces and antiphase defects, which are effective scatterers of heat-carrying phonons.

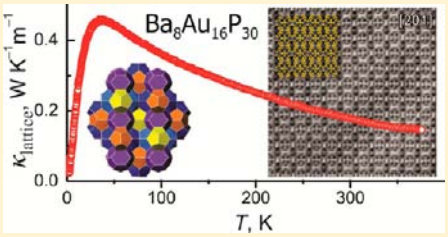

INTRODUCTION

The escalating demand for alternative clean energy sources requires the development of new and effective materials for energy recovery, conversion, storage, and transfer.[1] Thermoelectric (TE) materials convert heat into electric energy and vice versa and thus may help reduce our dependence on fossil fuels. Thermoelectric materials can be used for a wide range of applications such as Freon-free refrigerators and air conditioners and waste-heat and direct-solar thermal energy converters.[2] The performance of a TE material is expressed by the dimensionless figure of merit $ZT = TS^2/\rho\kappa$, where S is the thermopower (Seebeck coefficient), T is the absolute temperature, ρ is the electrical resistivity, and κ is the thermal conductivity. Thus, a TE material should be a good electrical conductor (low ρ) and induce a high voltage in response to a temperature gradient (high S) but should be a poor heat conductor (low κ) to maintain the applied temperature gradient.[2] State-of-the-art TE materials exhibit ZT values in the range of 1−2 depending on the application temperature.[2−5] Further increases in ZT are required for TE materials to become competitive with conventional heat-exchange systems. The main issue with engineering more efficient TE materials arises from the fundamental properties of solids: the parameters S, σ, and κ are strongly coupled and cannot be optimized independently.[2] Metals are inefficient TE materials because of their high thermal conductivities, while insulators exhibit very high electrical resistivities, decreasing their ZT values drastically.

The development of novel materials in which charge and heat transport are partially decoupled is a key factor for the next generation of TE materials. One effective approach to reduce the lattice thermal conductivity is to create thermoelectric nanocomposites that incorporate nanoparticle precipitates within a bulk matrix.[3] The most remarkable result of this approach was recently reported by Kanatzidis and co-workers,[4] who achieved a ZT of 2.2 at 915 K through a panoscopic approach to the scattering of heat-carrying phonons across

Received: May 25, 2013
Published: July 17, 2013

   dx.doi.org/10.1021/ja4052679 | J. Am. Chem. Soc. 2013, 135, 12313−12323

integrated length scales from atomic-scale lattice disorder and nanoscale endotaxial precipitates to mesoscale grain boundaries. A bottom-up approach to the synthesis of sulfur-doped bismuth telluride nanoplates achieved a remarkable ZT value of 1.1 at room temperature.[5]

Another approach, the "phonon glass−electron crystal" (PGEC) concept,[6] suggests the use of perfectly crystalline compounds containing loosely bonded atoms inside oversized cages. These materials are expected to have low thermal conductivities and low electrical resistivities. A widely studied class of PGEC compounds are clathrates, a class of inclusion compounds containing a three-dimensional framework with large cavities in which guest atoms are situated.[7] The first examples of intermetallic clathrates, sodium silicide clathrates, were reported in 1965.[8] Over the last 40 years, about 200 tetrel clathrates have been reported.[7] The term "tetrel" signifies that the clathrate framework is based on Si, Ge, or Sn. Only a few exceptions with clathrate frameworks composed of late transition metals (groups 11−12) and pnicogen (group 15) have been reported.[9] We believe that clathrates containing a high concentration of transition metals in the framework will exhibit structural chemistry and transport properties that are different from conventional tetrel-based clathrates. The introduction of a heavy transition metal such as gold should be beneficial for the reduction of the lattice thermal conductivity. In this work, we report how a combination of atomic and nanoscale complexity can be achieved in a single-phase material, resulting in an unprecedentedly low lattice thermal conductivity. The synthesis, crystal and electronic structures, and transport properties of the novel clathrate compound $Ba_8Au_{16}P_{30}$ are discussed.

EXPERIMENTAL SECTION

Synthesis. A single-phase sample of $Ba_8Au_{16}P_{30}$ was obtained from the solid-state reaction of its elements. All manipulations with the initial materials were performed inside an argon-filled glovebox [$p(O_2)$, $p(H_2O) \leq 1$ ppm]. The starting materials, metallic barium (Sigma-Aldrich, 99.9%), gold powder (Alfa Aesar, 99.96%), copper powder (Alfa Aesar, 99.99%), gold(I) chloride (Sigma-Aldrich, 99%), and red phosphorus (Alfa Aesar, 99%), were used as received. Ba, Au, and P were mixed in stoichiometric amounts, placed into glassy-carbon crucibles, and subsequently sealed inside evacuated silica ampules. The ampules were heated to 1073 K over 17 h and annealed at that temperature for 140 h. The products were then ground and annealed for 140 h under the same conditions.

Additionally, the synthesis of $Ba_8Au_{16}P_{30}$ was performed using AuCl as a flux. Ba, AuCl, and P were mixed in a 16:16:30 molar ratio and annealed at 1073 K for 140 h. Any barium chloride formed during the synthesis was removed by washing the sample with water. The annealed samples contained numerous silvery crystals that were stable in air for at least several months and resistant to a 24 h treatment with concentrated hydrochloric acid. A reference compound for NMR studies, $Ba_8Cu_{16}P_{30}$, was prepared by the standard technique described elsewhere.[9d]

Powder X-ray Diffraction. The samples were characterized by powder X-ray diffraction (PXRD) using a Bruker D8 Advance diffractometer employing Cu Kα radiation. High-resolution synchrotron powder diffraction data were collected at beamline 11-BM at the Advanced Photon Source (APS) at Argonne National Laboratory using an average wavelength of 0.41 Å. Discrete detectors covering a 2θ range from −6 to 16° were scanned over a 2θ range of 34°, with data points collected every 0.001° in 2θ at a scan speed of 0.01°/s. The $Ba_8Au_{16}P_{30}$ sample was mixed with amorphous silica to achieve reasonable transmission. Rietveld structural refinement of the powder diffraction data was performed using the JANA 2006 software.[10] Rietveld refinement (see Table 1) was used to minimize $\sum w_i(I_{o,i} - I_{c,i})^2$, where $I_{o,i}$ and $I_{c,i}$ are the observed and calculated powder diffraction intensities for the ith point, respectively. The weights w_i were set equal to $1/I_{o,i}$. The weighted and unweighted profile R factors are defined as $R_{wp} = [\sum w_i(I_{o,i} - I_{c,i})^2/\sum w_i(I_{o,i})^2]^{1/2}$ and $R_p = \sum|(I_{o,i} - I_{c,i})|/\sum I_{o,i}$, respectively. χ^2 is defined as the ratio of $R_{wp}/R_{expected}$, where the expected R factor (the best statistically possible value for R_{wp}) is defined as $R_{expected} = [(N - P)/\sum w_i(I_{o,i})^2]^{1/2}$, where N is the number of observed powder diffraction data points and P is the number of refined parameters.

Single-Crystal X-ray Diffraction. Multiple crystals of $Ba_8Au_{16}P_{30}$ produced from the stoichiometric syntheses and flux reactions were tested, and 10 data sets were collected. All of the crystals exhibited similar twinning issues. Room-temperature and 90 K single-crystal XRD experiments were carried out using a Bruker AXS SMART diffractometer with an APEX-II CCD detector and Mo Kα radiation. The data sets were recorded as ω scans with a 0.3° step width and integrated using the Bruker SAINT software package.[11] A multiscan adsorption correction was applied using TWINABS software.[12] The solution and refinement of the crystal structures were carried out using the SHELX suite of programs.[13]

Elemental Analysis. Elemental analyses of selected single crystals were carried out on a Hitachi S4100T scanning electron microscope with energy-dispersive X-ray microanalysis (Oxford INCA Energy). Sample analysis confirmed the presence of only Ba, Au, and P in the samples. Because of the overlap of the Au and P lines, the analysis was semiquantitative. The observed Ba:Au:P ratio of 18:31:52 was close to the theoretical one (15:30:56).

Transmission Electron Microscopy. Samples for transmission electron microscopy (TEM) were ground under ethanol, and the resulting dispersion was transferred to a lacey or holey carbon film fixed on a 3 mm copper grid. High-resolution TEM (HRTEM) and electron diffraction (ED) studies were performed using a Tecnai G2 30 UT (LaB_6) microscope operated at 300 kV with 0.17 nm point resolution. High-angle annular dark-field scanning TEM (HAADF-STEM) studies were performed using a Tecnai F20 field-emission gun electron microscope operated at 200 kV. Atomic models of defects were built using the CrystalMaker[14a] and Vesta[14b] software programs. HRTEM image simulations were performed using the MacTempas[14c] and CrystalKit[14d] software programs.

Solid-State ^{31}P NMR Spectroscopy. The ^{31}P magic-angle-spinning (MAS) NMR spectra of polycrystalline $Ba_8Au_{16}P_{30}$ were collected at spinning speeds of 10−18 kHz using a Bruker Avance 500 spectrometer operating at a resonance frequency of 202.4 MHz for ^{31}P. The crushed sample was placed in a ZrO_2 rotor and spun in a Bruker 2.5 mm MAS probe. The one-pulse ^{31}P MAS NMR spectra at different spinning speeds were obtained using a $\pi/4$ pulse (1 μs) and a recycle delay of 1 s. A total of 720 free induction decays were averaged and Fourier transformed to obtain the spectrum. Line shape simulation was performed using the DMfit software.[15] The ^{31}P chemical shift was externally referenced to that of 85% aqueous H_3PO_4.

Sample Densification. A powdered single-phase sample of $Ba_8Au_{16}P_{30}$ was compacted using spark plasma sintering. A 5 mm graphite pressure die with WC plungers was used. Samples were compacted at an applied temperature and pressure of 773 K and 90 MPa, respectively, and the pressed samples were polished to remove graphite. The resulting geometrical density was 92% of the theoretical X-ray density.

Physical Properties. Transport properties over the temperature range 2−390 K were studied using a commercial multipurpose measurement device (Quantum Design PPMS). The Seebeck coefficient and thermal conductivity were measured using the thermal transport option. Electrical resistivity was measured using a standard four-point alternating-current technique to exclude resistance of the leads.

RESULTS AND DISCUSSION

Synthesis. A single-phase sample of $Ba_8Au_{16}P_{30}$ was successfully synthesized from its elements using a two-step

dx.doi.org/10.1021/ja4052679 | J. Am. Chem. Soc. 2013, 135, 12313−12323

annealing process at 1073 K. Syntheses at a higher temperature of 1173 K resulted in the formation of another ternary compound, $BaAu_2P_4$.[16] Products of the reaction performed at a lower temperature of 973 K contained chunks of unreacted Ba with the surface passivated with barium phosphide. The melting temperature of barium is 1000 K.

Single-Crystal X-ray Diffraction. All of the studied single crystals revealed strong tendencies for twinning. Our attempts to improve the crystallinity by a prolonged (2 week) third annealing of the single-phase sample at 1073 K or by growing crystals from flux resulted in crystals of similar quality. We collected 10 experiments at different temperatures using crystals selected from different batches. All of the data sets were indexed in a body-centered-cubic (bcc) unit cell. Most of the reflections with intensity $I > 6\sigma(I)$ were indexed in a bcc unit cell with $a = 20.708(1)$ Å. Taking into account all of the reflections, including the weak ones, resulted in doubling of the unit cell parameter to $a = 41.399(3)$ Å. In both cases, multiple twinning components were present. With the assumption that $Ba_8Au_{16}P_{30}$ has a clathrate-I type of crystal structure, a crystal structure model was obtained with the help of the Bilbao Crystallographic Server[17] for a bcc unit cell in the $Im\bar{3}$ space group with $a = 20.708(1)$ Å. Refinement of the model resulted in joint occupancy of almost every crystallographic position of the clathrate framework by both Au and P atoms. Site occupancy factors for different framework positions varied from Au/P = 80/20 to 15/85. A final R_1 value of 6.6% was obtained. Refinement of other data sets resulted in similar models but with different Au/P occupancies for the framework positions.

The obtained model makes little chemical sense. The standard clathrate-I structure crystallizes in a primitive cubic unit cell with $a \approx 10$ Å and volume $V_0 \approx 1000$ Å^3. Different kinds of superstructures have been reported for clathrate-I compounds: $Sn_{14}In_{10}P_{21.2}\square_{0.8}I_8$ (tetragonal, $P4_2/m$, $V = 5V_0$), $Ba_8Ge_{43}\square_3$ and $A_8Sn_{44}\square_2$ (A = Rb, Cs) (cubic, $Ia\bar{3}d$, $V = 8V_0$), $Sn_{20.5}\square_{3.5}As_{22}I_8$ (cubic, $F23$, $V = 8V_0$), $[Ge_{46-x}P_x]Te_y$ (cubic, $Fm\bar{3}$, $V = 8V_0$), and $Ba_8Cu_{16}P_{30}$ (orthorhombic, $Pbcn$, $V = 4V_0$).[9a,18] In all cases, the superstructure formation is accompanied by partial or full ordering of either vacancies or atoms of different chemical nature (e.g., Cu and P in the case of $Ba_8Cu_{16}P_{30}$) in the clathrate framework. In the case of $Ba_8Au_{16}P_{30}$, an increase in the unit cell volume would be expected to result from ordering of the Au and P atoms in the framework positions, since there are no vacancies in this clathrate. However, the refined model showed no ordering. Moreover, the Au/P ratio for the same crystallographic position varied from crystal to crystal. Since heavy twinning was observed, we performed ED and high-resolution PXRD studies.

High-Resolution PXRD and ED Studies. The ED pattern of the pseudo-cubic zone [111] is shown in the Figure 1a inset. The intense diffraction spots (marked by white circles) exhibit threefold rotational symmetry. However, the low-intensity spots (marked by white arrowheads) clearly violate threefold rotational symmetry, indicating the absence of cubic symmetry. The high-resolution PXRD pattern could not be indexed in either the cubic unit cell with $a = 20.708(1)$ or the cubic unit cell with $a = 41.399(3)$ Å. These findings clearly indicated that the model obtained from the single-crystal XRD data was incorrect. Indexing of the powder pattern was performed using the TREOR software.[19] The resulting unit cell was found to have orthorhombic symmetry with $a = 14.6362(1)$ Å, $b = 10.4655(1)$ Å, $c = 28.9836(2)$ Å. This corresponds to a $\sqrt{2}a_{subcell} \times a_{subcell} \times 2\sqrt{2}a_{subcell}$ superstructure of the prototype

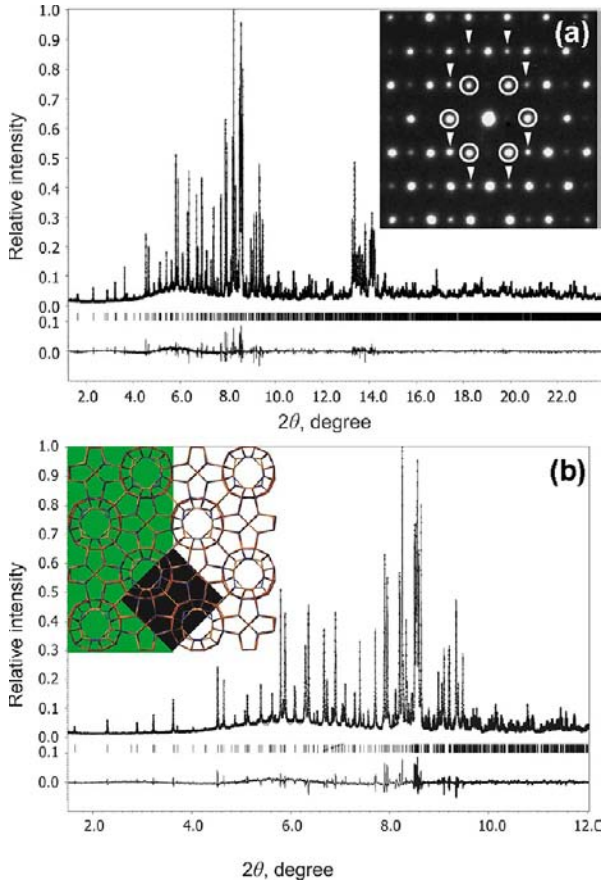

Figure 1. (a) PXRD pattern ($2\theta = 0$–$24°$) and corresponding Rietveld refinement (black line) of the PXRD data (black •) for $Ba_8Au_{16}P_{30}$ collected at room temperature. Black marks indicate the theoretical Bragg peak positions. The difference is shown as a curve at the bottom. The ED pattern of the pseudo-cubic [111] zone of $Ba_8Au_{16}P_{30}$ is given in the inset. Circles indicate spots that satisfy threefold symmetry, whereas triangular arrowheads indicate reflections that violate threefold rotation. (b) Low-angle portion of the PXRD pattern. The inset shows the $Ba_8Au_{16}P_{30}$ framework. The superstructure and substructure cells are indicated by green and black rectangles, respectively.

clathrate-I unit cell. A similar type of superstructure was reported for $Ba_8Cu_{16}P_{30}$.[9a] The atomic coordinates and space group $Pbcn$ (No. 60) of the latter compound were used as the initial model for refinement of the crystal structure of $Ba_8Au_{16}P_{30}$ from PXRD data. In the final stage of refinement, the occupancy of each atomic position was refined independently in separate refinement cycles. All of the atomic positions exhibited no deviation from 100% occupancy within 1 estimated standard deviation. The final refinement converged to $R_p = 5.1\%$ and $\chi^2 = 1.67$ (Figure 1). Details of the data collection and structure refinement parameters for $Ba_8Au_{16}P_{30}$ are given in Table 1. Atomic coordinates, displacement parameters, and bond lengths are given in Tables SI 1 and SI 2 in the Supporting Information.

Refinement of the single-crystal data in the correct orthorhombic superstructure still resulted in joint occupancy of almost every crystallographic position of the clathrate framework by both Au and P atoms, probably because of the presence of multiple twinned components (vide infra).

Crystal Structure. In the crystal structure of $Ba_8Au_{16}P_{30}$, gold and phosphorus atoms form the clathrate-I framework. Ba

dx.doi.org/10.1021/ja4052679 | J. Am. Chem. Soc. 2013, 135, 12313–12323

Table 1. Data Collection and Refinement Parameters for the Structure Determination of $Ba_8Au_{16}P_{30}$[a]

composition	$Ba_8Au_{16}P_{30}$	λ (Å)	0.41335
space group	*Pbcn* (No. 60)	ρ (g cm^{-3})	7.746
T (K)	293(2)	μ (mm^{-1})	14.689
a (Å)	14.6362(1)	2θ (deg)	$0.5 < 2\theta < 40.0$
b (Å)	10.4655(1)	R_p	0.051
c (Å)	28.9836(2)	R_{wp}	0.069
V (Å^3)	4439.57(6)	R_{exp}	0.041
Z	4	χ^2	1.67

[a]Further details of the crystal structure determination may be obtained from Fachinformationszentrum Karlsruhe, D-76344 Eggenstein-Leopoldshafen, Germany, upon quotation of the depository number CSD-426104.

atoms are situated inside the large cages of the framework. $Ba_8Au_{16}P_{30}$ is isostructural to the Cu-containing analogue, $Ba_8Cu_{16}P_{30}$, and exhibits the same type of clathrate-I superstructure (Figure 1b inset). The formation of the superstructure is caused by the ordering of gold and phosphorus atoms within different framework positions. In $Ba_8Au_{16}P_{30}$, each gold atom is tetrahedrally coordinated by four phosphorus atoms. We recently showed that the orthorhombic $\sqrt{2}a_{subcell} \times a_{subcell} \times 2\sqrt{2}a_{subcell}$ clathrate-I superstructure in the space group *Pbcn* is a way to order 16 metal and 30 phosphorus atoms within the clathrate framework, avoiding the formation of metal−metal bonds or, in other terms, maximizing the Au−P interactions.[9d]

The type-I clathrate structure contains two types of polyhedral cages, 20-vertex pentagonal dodecahedra [5^{12}] and larger 24-vertex, 14-face tetrakaidecahedra [$5^{12}6^2$] (see ref 20 for polyhedra notation). In the framework of $Ba_8Au_{16}P_{30}$, five crystallographically independent cages are formed: two pentagonal dodecahedra and three tetrakaidecahedra (Figure 2). Gold and phosphorus atoms are not equally distributed over the different polyhedra: shown in blue are phosphorus-rich Au_6P_{14} pentagonal dodecahedra, while gold-rich Au_8P_{12} units are shown in yellow. Similarly, the larger tetrakaidecahedra have either Au_8P_{16} or Au_9P_{15} compositions. All of the polyhedra are filled with barium atoms. The shortest Ba−P and Ba−Au distances are 3.25 and 3.30 Å, respectively.

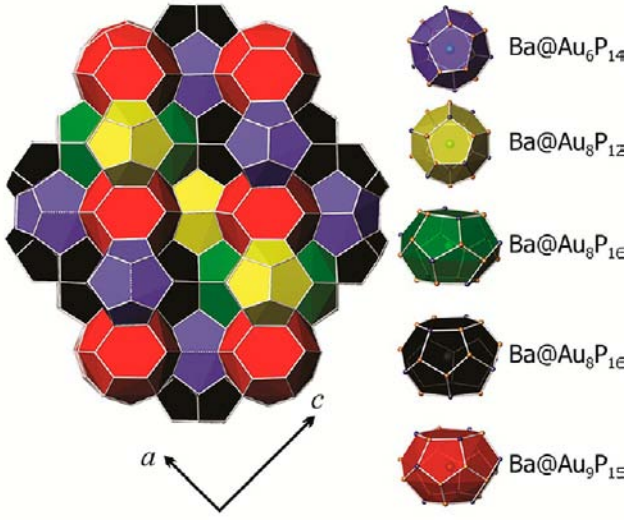

Figure 2. Polyhedral representation of the crystal structure of $Ba_8Au_{16}P_{30}$. The polyhedron color legend is given on the right. In the legend, Au atoms are shown in blue and P atoms in brown. P15−P15 bonds (see the text) are shown as dotted lines.

$Ba_8Au_{16}P_{30}$ is the first example of a clathrate with 35% of the framework built from a period-6 element, gold. Several clathrates containing period-6 elements (Au, Hg, Bi) were previously reported,[21] but the concentrations of these elements did not exceed 13%. The presence of heavier elements should be beneficial for reducing the thermal conductivity of the $Ba_8Au_{16}P_{30}$ clathrate.

In the crystal structure of $Ba_8Au_{16}P_{30}$, the Au−P distances are similar to those in other binary and ternary gold phosphides (Tables SI 2 and SI 3 in the Supporting Information). It should be noted that tetrahedral coordination is not typical for gold−phosphorus fragments. In most compounds, either linear AuP_2 or trigonal-planar AuP_3 fragments are found (Table SI 3). This differentiates gold from copper, for which tetrahedral CuP_4 fragments are typical (e.g., in CuP_2 or Cu_2P_7).[22] In Au_2P_3, each gold atom is linearly coordinated by two phosphorus atoms.[23]

Unlike gold atoms, phosphorus atoms form homoatomic bonds. The local coordination of phosphorus ranges from three Au and one P to one Au and three P. The P−P bond lengths vary from 2.12 to 2.42 Å, which is typical for single P−P bonds.[24] However, the P15−P15 distance (2.72 Å) is an exception (Figures 2 and 3). In the isostructural Cu-containing

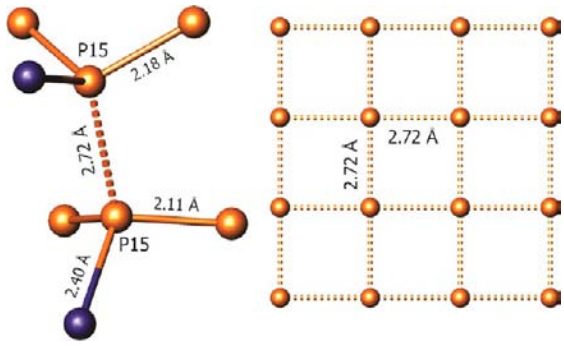

Figure 3. (left) Local coordination of P15 atoms in the crystal structure of $Ba_8Au_{16}P_{30}$. (right) Square net of distant phosphorus atoms found in $SmCuP_2$. P, brown; Au, blue.

analogue, $Ba_8Cu_{16}P_{30}$, the distance between corresponding phosphorus atoms is shorter (2.46 Å).[9a,d] Analyses of the difference electron density maps indicated that this is the true position for P15 atoms in the crystal structure and not an artifact of Rietveld refinement. The refinement of the occupancy of P15 clearly showed that this position is exclusively occupied by phosphorus. The distance of 2.72 Å is significantly longer than the sum of the covalent radii (2.20 Å).[25] Similar long homoatomic phosphorus bonds are found in planar phosphorus square nets in the compounds $SmCuP_2$ (2.72 Å)[26] and UP_2 (2.69 Å)[27] (Figure 2). Square networks with elongated pnicogen−pnicogen distances are more typical for heavier pnicogens such as Sb and Bi.[28]

According to the Zintl concept[29,30] each barium atom donates two electrons to the framework, becoming Ba^{2+}. Each Au and P framework atom requires four electrons for the formation of two-center−two-electron bonds, giving a total of $46 \times 4 = 184$ electrons per formula unit. If it is assumed that Au atoms have a closed-shell d^{10} configuration, gold and phosphorus atoms are expected to provide one and five valence electrons, respectively. The total number of electrons per formula unit is $(8 \times 2) + (16 \times 1) + (30 \times 5) = 182$

dx.doi.org/10.1021/ja4052679 | J. Am. Chem. Soc. 2013, 135, 12313−12323

electrons, which is two fewer electrons than required for the structure to be electron-balanced according to the Zintl counting scheme. Violation of the Zintl electron balance should result in $Ba_8Au_{16}P_{30}$ having metallic properties with holes as the main charge carriers.

Another way to describe the electronic structure of this compound is to assume full polarization of the Au−P bonds, with each gold atom in the form of a stable Au^+ cation and each phosphorus atom gaining an electron octet by accepting all of the electrons donated by Ba and Au atoms. This description was shown to work well for the prediction of the properties of $BaAu_2P_4$.[16] In $Ba_8Au_{16}P_{30}$, three different types of P atoms can be identified in the phosphorus substructure: three-bonded atoms (3*b*-P) coordinated to three other phosphorus atoms should be P^0, two-bonded atoms (2*b*-P) coordinated to two other phosphorus atoms should be P^-, and one-bonded atoms (1*b*-P) coordinated to only one other phosphorus should be P^{2-}. The general composition should be written as $(Ba^{2+})_8(Au^+)_{16}(3b\text{-}P^0)_2(2b\text{-}P^-)_{22}(1b\text{-}P^{2-})_6{\cdot}2h^+$, which is still missing two electrons. Each P15 atom forms a long bond (2.72 Å) with another P15 atom and two conventional bonds with other phosphorus atoms (Figure 3). Thus, P15 atoms are formally P^0. The assumption that the P15−P15 separation corresponds to a nonbonding pair of atoms would correspond to the reduction of the P15 atoms to the P^- formal oxidation state. This would lead to an even less balanced composition, $(Ba^{2+})_8(Au^+)_{16}(2b\text{-}P^-)_{24}(1b\text{-}P^{2-})_6{\cdot}4h^+$. To clarify the phosphorus bonding, we studied $Ba_8Au_{16}P_{30}$ by ^{31}P MAS solid-state NMR spectroscopy.

^{31}P MAS Solid-State NMR Spectroscopy. ^{31}P MAS NMR spectra of the polycrystalline $Ba_8Au_{16}P_{30}$ sample were collected at different spinning speeds, and a representative spectrum is shown in Figure 4. NMR simulations were carried out on multiple spectra collected at various spinning speeds, which enabled unambiguous determination of four distinct isotropic peak positions. The chemical shift anisotropies were determined by simultaneous fitting of the sideband intensities of the spectra using the Herzfeld−Berger method. The spectrum shown in Figure 4 is characterized by multiple resonances with isotropic chemical shifts in the range 332−755 ppm (Table 2). These chemical shifts are located at significantly higher frequencies than the typical range reported for electron-balanced diamagnetic phosphides (0 to −300 ppm).[16] The observed large paramagnetic deshielding of the chemical shifts in $Ba_8Au_{16}P_{30}$ is indicative of Fermi contact or pseudocontact shift interactions of the nuclear magnetic moments with a nonzero delocalized density of unpaired electron spins, or by a Knight shift from conduction electrons, thus confirming the paramagnetic nature of the studied compound. Similar high ^{31}P chemical shifts were observed for the paramagnetic phases $LaIr_2P_2$ and R_2AuP_2O (R = La−Nd).[31]

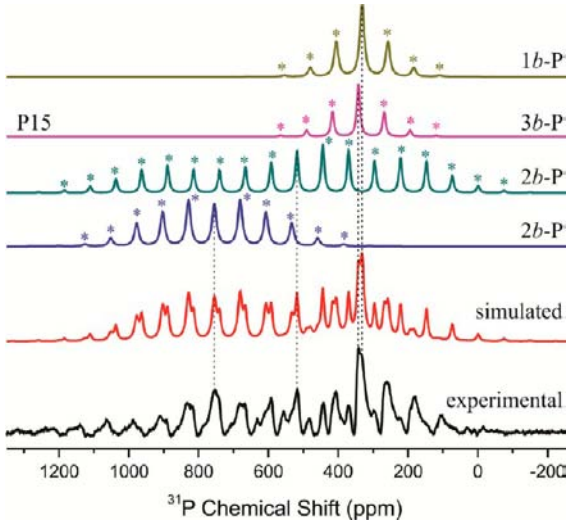

Figure 4. ^{31}P MAS NMR spectrum of $Ba_8Au_{16}P_{30}$. From bottom to top: experimental spectrum collected at a spinning speed of 15 kHz (black); sum of the simulated line shapes (red); and four simulated individual components. Isotropic chemical shifts are shown with dashed lines, and asterisks denote spinning sidebands in the simulated components.

Table 2. Chemical Shifts and Relative Intensities of the ^{31}P NMR Signals for $Ba_8Au_{16}P_{30}$

type of P atom	structural ratio	δ (ppm)	relative intensity
1*b*-P: 3Au+P	6	332	6
2*b*-P: 2Au+2P	22	755, 518	22
3*b*-P: 1Au+3P	2	342	3

The ^{31}P NMR line shape of $Ba_8Au_{16}P_{30}$ is complicated by the presence of multiple crystallographic phosphorus sites in the crystal structure together with large shift anisotropies resulting from paramagnetic interactions that give rise to spinning sideband manifolds covering the ∼200 kHz frequency range. It should be noted that the peaks shifted to higher frequencies (more positive shifts) have the largest paramagnetic shift anisotropy. Phosphorus atoms of the 2*b* type are the most deshielded because they have the highest free electron density on or near the ^{31}P nuclide. Moreover, these phosphorus atoms exhibit two resonances with quite distinct chemical shifts. Phosphorus atoms in $Ba_8Au_{16}P_{30}$ form two finite polyphosphide fragments, P_{12} and P_{18} (Figure SI 1 in the Supporting Information), and 2*b*-P atoms from different fragments may exhibit different chemical shifts. However, the 1*b*-P atoms terminating both fragments exhibit similar chemical shifts that were not resolved in the current study.

To clarify the chemical bonding of the P15 atoms (Figure 3), ^{31}P MAS NMR characterization of the isostructural copper analogue, $Ba_8Cu_{16}P_{30}$, was performed (Table SI 4 in the Supporting Information). The 2*b*-P and 1*b*-P atoms in $Ba_8Cu_{16}P_{30}$ exhibit high chemical shifts similar to those in $Ba_8Au_{16}P_{30}$. In the copper-containing compound, the 1*b*-P atoms exhibit two contributions to the NMR spectrum, thus confirming the assumption of different shifts for the phosphorus atoms from different polyphosphide fragments. The most striking difference between the Cu- and Au-containing compounds is the chemical shift of the 3*b*-P atoms, P15. In $Ba_8Cu_{16}P_{30}$, P15 has a chemical shift of 51 ppm and d(P15−P15) = 2.46 Å, while in $Ba_8Au_{16}P_{30}$, P15 has a chemical shift of 342 ppm and d(P15−P15) = 2.72 Å. In the copper compound, the free electron density on P15 atoms is minimal, in accordance with the formal P^0 oxidation state for 3*b*-P atoms. This is additionally supported by the small chemical shift anisotropy of ∼200 ppm, compared with anisotropies of 500−700 ppm for the other positions. The significant deshielding of the P15 atoms in $Ba_8Au_{16}P_{30}$ upon elongation of the P15−P15 bonds is due to the increase in free electron density on these nuclei. This corresponds to the breaking of the P−P bond and formal reduction of the

dx.doi.org/10.1021/ja4052679 | J. Am. Chem. Soc. 2013, 135, 12313−12323

phosphorus atoms to P^{-}. Thus, NMR spectroscopy indicates that the long P15−P15 distance of 2.72 Å corresponds to an essentially nonbonding interaction, and in the $Ba_8Au_{16}P_{30}$ compound, the P15 atoms should be considered as formally bonded to only two phosphorus atoms. Framework bond breaking was previously observed in the germanium-containing clathrate Ba_6Ge_{25}.[32]

The measured ^{31}P spin−lattice relaxation times (T_1 = 40 and 10 ms for the Au- and Cu-containing compounds, respectively) are extremely short relative to the typical long relaxation times of 1−50 s characteristic of diamagnetic, electron-balanced compounds. This is additional confirmation of the paramagnetic nature of the studied material.

Transmission Electron Microscopy. TEM was applied to confirm the structural model obtained from PXRD. TEM is a very powerful tool for the investigation of the local structure of clathrates.[18,33] Figure 5 shows ED patterns along the main

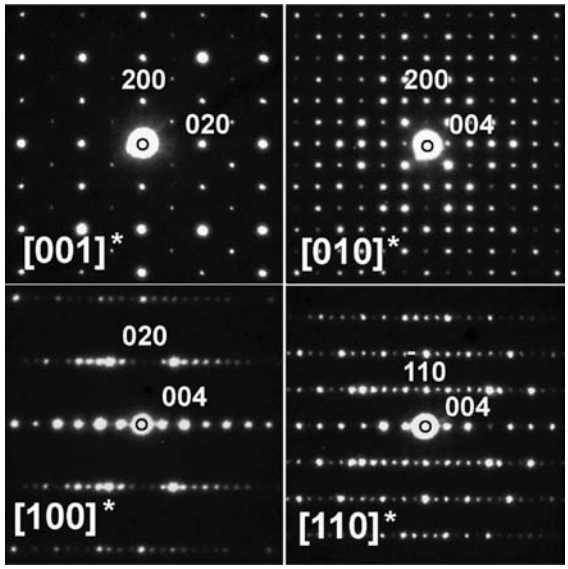

Figure 5. ED patterns along the main zones [001], [010], [100], and [110] of $Ba_8Au_{16}P_{30}$.

[001], [010], [100], and [110] zones. The diffraction patterns can be completely indexed in the *Pbcn* space group using the unit cell parameters determined by PXRD (Table 1). An HRTEM study was performed along the most informative zones.

All of the HRTEM images exhibited uniform contrast free of any modulation and defects within the single crystallite, indicating a perfectly ordered crystal structure for the $Ba_8Au_{16}P_{30}$ clathrate. The calculated images for different zones, thicknesses, and defocus volumes were in good agreement with the experimental HRTEM images (Figure 6). No features resulting from long-range or short-range atom or vacancy ordering were observed.

The combination of HRTEM and ED is a powerful technique for unraveling and determining complex structures. However, the direct interpretation of HRTEM images of a complex compound with a large unit cell is not always straightforward because of electron−matter interactions. In addition, HRTEM is not very sensitive to small compositional variations within one atomic column. To overcome these drawbacks, HAADF-STEM was used to verify the crystal structure model of $Ba_8Au_{16}P_{30}$ and determine possible

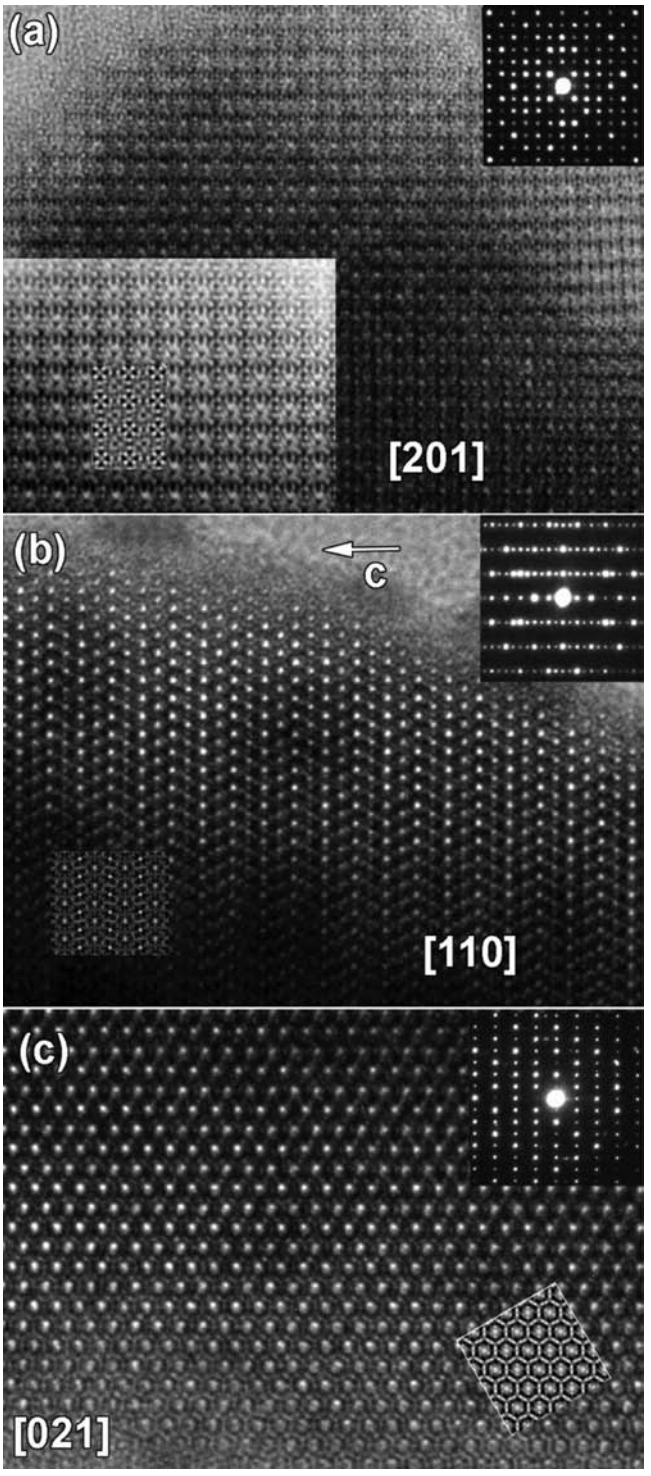

Figure 6. HRTEM images along the most informative zones for $Ba_8Au_{16}P_{30}$: (a) [201]; (b) [110]; (c) [021]. The corresponding ED patterns are shown in the upper-right insets. The calculated images [(a) t = 4 nm, Δf = −30 nm; (b) t = 4 nm, Δf = −60 nm; (c) t = 6 nm, Δf = −50 nm] based on the structural model (Table 1 and Table SI 1 in the Supporting Information) are shown in the lower insets.

structural or/and compositional variations at the atomic level. The contrast in HAADF-STEM is roughly proportional to the mean-square atomic number ($\sim Z^2$), making it possible to detect small changes in Au (Z = 79) and Ba (Z = 56) composition and positions. Figure SI 2 in the Supporting Information shows HAADF-STEM images of $Ba_8Au_{16}P_{30}$ along

dx.doi.org/10.1021/ja4052679 | J. Am. Chem. Soc. 2013, 135, 12313−12323

the main zone axis. There is a good fit between the experimental images and the overlapped atomic models. No detectable contrast variations at Au and Ba positions were observed, suggesting a perfect structure free of compositional and structural variations. This result is in good agreement with the HRTEM observations. Nevertheless, certain problems occurred during single-crystal XRD data interpretation.

Macroscopic defects in $Ba_8Au_{16}P_{30}$ may be responsible for the difficulties in the single-crystal XRD data analysis. The HRTEM, HAADF-STEM, and ED studies provided a clear answer to the question of why all of the single-crystal XRD experiments failed. $Ba_8Au_{16}P_{30}$ exhibits quite a number of extended defects, such as antiphase boundaries (APBs) and twinning with pseudo-three- and -fourfold rotational axes. The latter symmetry elements are present in the ideal clathrate-I structure but are absent in the observed orthorhombic superstructure of $Ba_8Au_{16}P_{30}$.

Threefold rotational twinning is clearly seen in the ED pattern, which contains reflections that violate threefold-axis hexagonal symmetry (Figure 1a inset). Figure 7a shows three selected-area ED (SAED) patterns (A, B, and C) taken from different areas of the same single crystallite that are rotated 120° along the [021] axis with respect to each other. It should be noted that those diffraction spots satisfying threefold symmetry (depicted with a hexagon) remain in their positions. The resulting ED pattern taken from all three areas of the crystallite (bottom-left inset in Figure 7a) is the superposition of the three ED patterns along the [021]* zone and exhibits pseudo-threefold rotational symmetry. The corresponding structural model is shown in Figure 7a and consists of three [021] domains of $Ba_8Au_{16}P_{30}$ (white, pink, and gray). The twin boundary is coherent and almost invisible in the HRTEM image along [021] zone axis because of the pseudohexagonal symmetry, resulting in a perfect hexagonal HRTEM image (Figure 6c). Since the domains are rotated with respect to each other, the twin boundary can be visualized easily along another crystallographic direction where two complementary domains should have different orientations. In the high-resolution HAADF-STEM image of a 120° rotational twin boundary along the [010] zone axis (Figure 7b left), the twin boundary parallel to the (001) plane is clearly visible because of the differently oriented domains: the bottom domain is [010] and top one is [201]. On the basis of the fine structure of the HAADF-STEM image, we can propose a structural model for the 120° rotational twin boundary (Figure 7b right). This model is a special case of the general model presented in Figure 7a.

Another type of twinning is the fourfold rotational twinning. An HRTEM image of a perfectly coherent twin boundary is shown in Figure 8. Two differently oriented domains, [100] and [001], are perfectly intergrown through a 90° rotation along the *b* axis. On the basis of the Fourier transform (FT) patterns, the following relationship between the two domains was developed: $[001]_A//[100]_B$, $[010]_A//[010]_B$, and $[100]_A//[001]_B$. Because of the presence of a superstructure in $Ba_8Au_{16}P_{30}$, the (100) and (001) planes exhibit very high

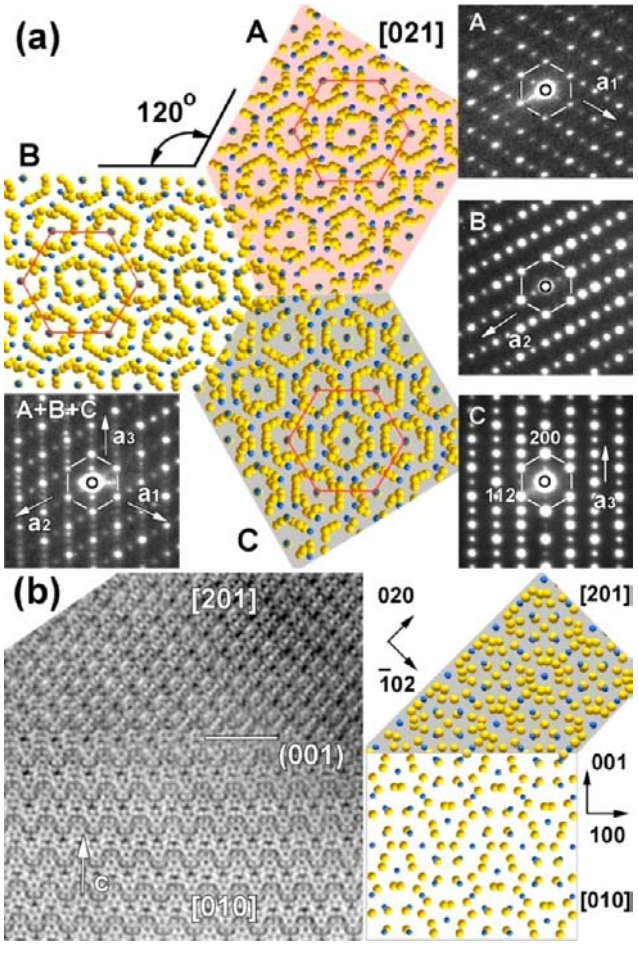

Figure 7. (a) [021] ED pattern taken from a single crystallite (bottom left corner) and SAED patterns A, B, and C taken from different areas of the same crystallite along the same [021]* zone axis (right). The 120° rotation of the *a* axis should be noted. A structural model for this type of rotational twinning is also shown (Au, yellow; Ba, blue). (b) High-resolution HAADF-STEM image of a selected twin boundary viewed along the [010] direction of one of the domains (left) and corresponding model (right).

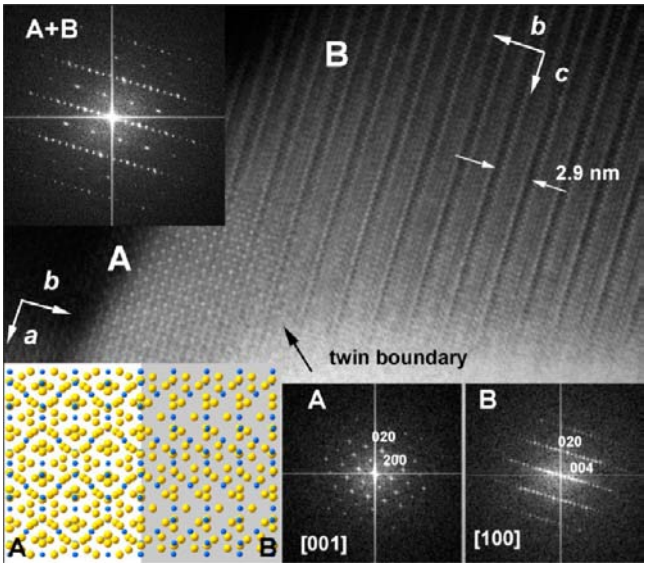

Figure 8. HRTEM image of the rotational twinning in $Ba_8Au_{16}P_{30}$. Two perfectly ordered parts, marked as "A" and "B", correspond to the [001] and [100] zones, respectively. FT patterns taken from parts A and B (bottom right corner), and the intergrowth region A+B (top left corner) are also shown. A structural model describing a 90° rotational twin along the [010] direction is given in the bottom left corner (Au, yellow; Ba, blue).

dx.doi.org/10.1021/ja4052679 | J. Am. Chem. Soc. 2013, 135, 12313−12323

structural similarity that results in coherent interfaces, as is evident from the HRTEM image (Figure 8).

In addition to different types of twinning and intergrowths, APB defects are also often observed. An APB defect occurs when the grains on either side of the boundary have the same orientation but are translated with respect to each other. Figure 9 shows high-resolution HAADF-STEM images of an APB

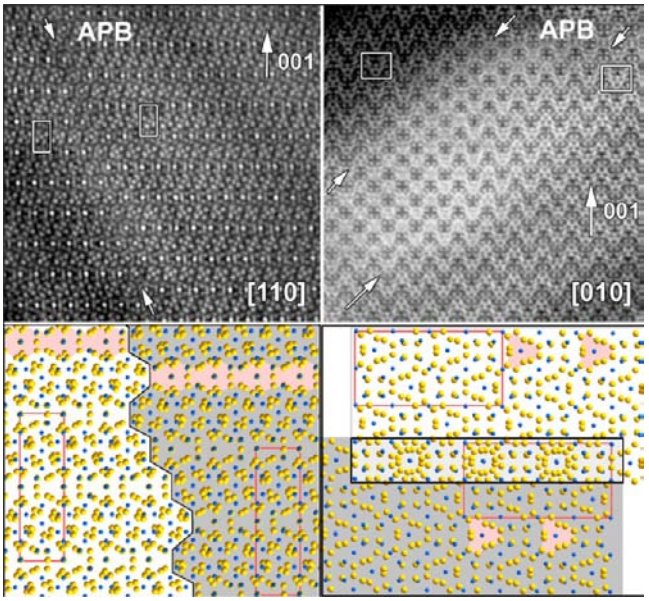

Figure 9. (top) High-resolution HAADF-STEM images of an APB along the [110] and [010] directions. (bottom) Corresponding structural models (Au, yellow; Ba, blue). Different parts of the crystal in the models have different background colors (gray and white). Identical parts of the structure are highlighted in pink. The boundaries are marked by black lines. Unit cells are shown with red rectangles.

defect viewed along two main directions: [110] and [010]. This allowed us to do a 3D reconstruction of the APB, and the resulting translation vector **R** between the two grains measured from these HAADF-STEM images can be expressed as **R** = $^1/_4$[001] + $^1/_2$[100]. The bright dots in the image correspond to the Au atomic columns, while darker dots are Ba atomic columns. The HAADF-STEM image of the APB along [110] clearly demonstrates that the APB does not follow a simple crystallographic direction and is roughly parallel to the $(\bar{1}11)$ plane. Therefore, the APB viewed along the [010] direction is no longer parallel to the electron beam and exhibits complex contrast due to overlap of the two crystals, a so-called moiré pattern. Taking into account the crystallographic and structural properties of $Ba_8Au_{16}P_{30}$ and the contrast of the APB from the experimental HAADF-STEM images (Figure 9), we can propose a model for the APB. The Ba atoms in this model are perfectly coincident, while the Au atoms are slightly shifted, which is associated with the rearrangement of phosphorus atoms along the APB. Moreover, the high-resolution HAADF-STEM images clearly show that the APB exhibits a zigzag configuration on the atomic scale and is faceted with $(\bar{1}10)$ and $(11\bar{1})$ planes.

The observed variety of structural defects, including three- and fourfold rotational coherent twinning, structural intergrowth, and APBs, should result in violations of the local coordination of Au and P atoms at the interfaces, which is supported by the HRTEM and HAADF-STEM observations and the proposed models. The appearance of the crystallographically prohibited interfaces results in the formation of homoatomic Au−Au bonds and possibly of local distortions of the coordination of Au atoms (i.e., deviations from tetrahedral coordination). The resolution of the electron microscopy used in the current study was not sufficient to investigate the local atomic distortion at the interfaces. Indeed, tetrahedral coordination by four phosphorus atoms is not typical for Au (vide supra) but is typical for Cu. For the copper analogue, $Ba_8Cu_{16}P_{30}$, no twinning was reported, and single-crystal XRD experiments unambiguously revealed the orthorhombic symmetry of this compound.[9a,d] We hypothesize that the prevalent twinning in $Ba_8Au_{16}P_{30}$ is caused by the tendency of gold atoms to relax from the constrained tetrahedral coordination. The thermal behavior of $Ba_8Au_{16}P_{30}$ is additional proof for this hypothesis: all of our syntheses at temperatures above 1123 K resulted in the formation of another compound with close composition, $BaAu_2P_4$ (which gives $Ba_8Au_{16}P_{32}$ when multiplied by 8).[16] In this compound, Au atoms exhibit strongly distorted tetrahedral coordination with two short bonds to P atoms (2.36 Å) and two bonds to more distinct Au atoms (3.22 Å).

The formation of twinning intergrowth structures is natural for $Ba_8Au_{16}P_{30}$ and is independent of the synthetic method. Several annealings with regrinding of the sample did not eliminate the twinning. Crystals grown from flux also exhibited similar twinning. The presence of coherent nanoscale interfaces should not affect charge-carrier transport but may significantly scatter heat-carrying phonons, thus reducing the thermal conductivity. The sizes of fully ordered crystallites varied from 20 to 500 nm (Figure SI 3 in the Supporting Information), which is larger than the typical size of nanoinclusions observed in PbTe-based materials.[3,4]

Thermoelectric Properties. The temperature dependences of the resistivity and Seebeck coefficient as well as the power factor $P = S^2/\rho$ for $Ba_8Au_{16}P_{30}$ are shown in Figure 10. The positive sign of the Seebeck coefficient indicates that holes are the main charge carriers, as expected from the Zintl count. The deviation from electron balance resulted in a metallic-like temperature dependence of the resistivity and a relatively small absolute value of the Seebeck coefficient. For $Ba_8Au_{16}P_{30}$, the thermoelectric figure of merit is ZT = 0.01 at 390 K. Optimization of the charge-carrier concentration aiming at an electron-balanced compound with a higher Seebeck coefficient is currently underway.

Despite its metal-like electrical conductivity, $Ba_8Au_{16}P_{30}$ exhibits a very low total thermal conductivity of 0.6 W m^{-1} K^{-1} (Figure 11). The thermal conductivity exhibits a maximum at ∼50 K, which is typical for crystalline solids and was observed for other Ba clathrates such as $Ba_8Ga_{16}Ge_{30}$ and $Ba_8Cu_{16}P_{30}$. No glass-like behavior typical for β-$Ba_8Ga_{16}Sn_{30}$ was detected in $Ba_8Au_{16}P_{30}$.[34−39]

The charge-carrier contribution to the thermal conductivity can be estimated from the Wiedemann−Franz law, $\kappa_{electronic} = L_0T/\rho$, where the ideal Lorentz number is calculated as $L_0 = {}^1/_3(\pi k_B/e)^2$. The lattice contribution to thermal conductivity ($\kappa_{lattice}$) was estimated by subtracting $\kappa_{electronic}$ from κ_{total} (Figure 11). The room-temperature (300 K) value of 0.18 W m^{-1} K^{-1} for $\kappa_{lattice}$ is unprecedentedly low. For comparison, the total and lattice thermal conductivities for the Cu-containing analogue at room temperature are 3.6 and 2.9 W m^{-1} K^{-1}, respectively.[39] Generally, for the majority of clathrates, $\kappa_{lattice}$ at room temperature is ∼1 W m^{-1} K^{-1}, and for certain compounds it

dx.doi.org/10.1021/ja4052679 | J. Am. Chem. Soc. 2013, 135, 12313−12323

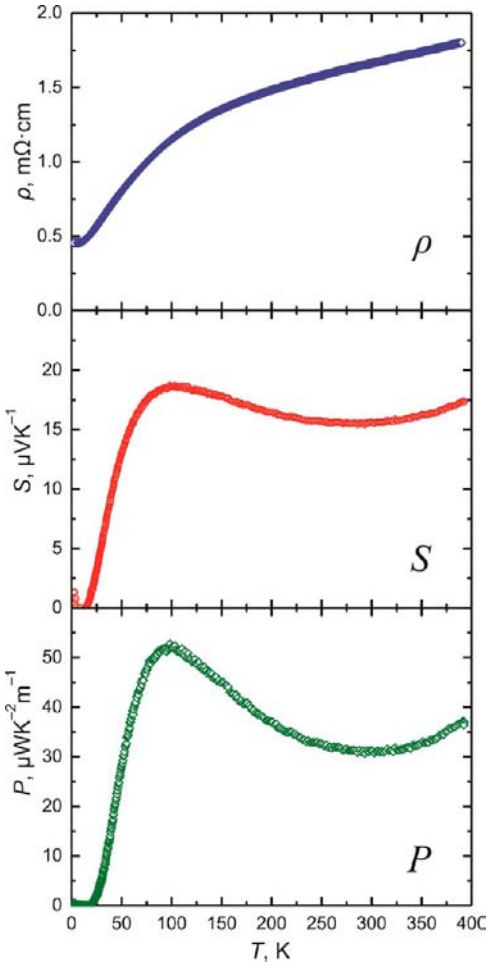

Figure 10. Temperature dependences of resistivity (ρ), Seebeck coefficient (S), and power factor (P) for $Ba_8Au_{16}P_{30}$. For each of the measured parameters, the estimated standard deviations were smaller than the symbol used.

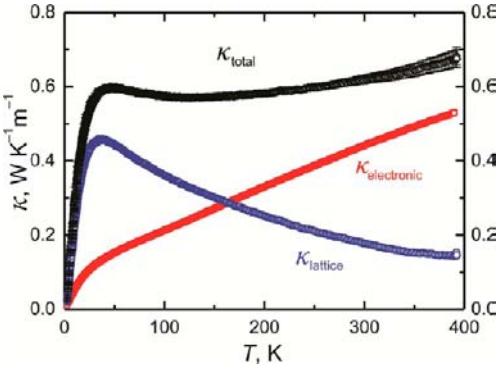

Figure 11. Total (black), electronic (red), and lattice (blue) thermal conductivities of $Ba_8Au_{16}P_{30}$.

decreases to 0.5 W m^{-1} K^{-1}.[6,7] It should be noted that low thermal conductivity is accompanied with a high degree of structural disorder that results in glasslike thermal conductivity behavior, unlike $Ba_8Au_{16}P_{30}$. For other classes of thermoelectric materials, a brief summary of room-temperature $\kappa_{lattice}$ values was recently reported.[40] The intermetallic compounds Ag_9TlTe_5 and $Gd_{117}Co_{56}Sn_{112}$ exhibit the lowest values of $\kappa_{lattice}$ (0.28 and 0.23 W m^{-1} K^{-1}, respectively).[40,41] The $R_{117}Co_{56}Sn_{112}$ intermetallic compounds exhibit a complex crystal structure with a giant unit cell and additional structural disorder at several atomic positions.[42] In contrast, $Ba_8Au_{16}P_{30}$ is fully ordered on the atomic level, as revealed by HRTEM and HAADF-STEM. The complex crystal structure and the presence of the large number of heavy atoms in the unit cell makes $Ba_8Au_{16}P_{30}$ similar to Ag_9TlTe_5. Below we estimate the impact of nanoscale interface defects on the properties of $Ba_8Au_{16}P_{30}$.

According to the PGEC concept,[6] heat-carrying phonons in the clathrate structure are mainly scattered by guest atoms, while the framework has less of an impact on the thermal conductivity. A comparison of data for Ge- and Sn-based clathrates with Ba guest atoms (Table 3) indicates that

Table 3. Values of Lattice Thermal Conductivity ($\kappa_{lattice}$) at 100 K, Change in Unit Cell Volume (ΔV), and Average Framework-Atom Mass (M_{av}) for Selected Clathrates

compound	$\kappa_{lattice}$ (W m^{-1} K^{-1})	ΔV (%)	M_{av} (amu)	refs
$Ba_8Ga_{16}Ge_{30}$	1.0−1.5	0[a]	72	34−36
β-$Ba_8Ga_{16}Sn_{30}$	0.7−0.9	+36[a]	102	34, 37, 38
$Ba_8Cu_{16}P_{30}$	2.0	0[b]	42	9a, 39
$Ba_8Au_{16}P_{30}$	0.36	+11[b]	89	this work

[a]Relative to $Ba_8Ga_{16}Ge_{30}$. [b]Relative to $Ba_8Cu_{16}P_{30}$.

clathrates with heavier framework atoms exhibit lower thermal conductivities. Thus, the substitution of Ga−Sn with Ga−Ge in the clathrate framework resulted in the reduction of $\kappa_{lattice}$ by ~50% (Table 3). This might be explained by two factors: (i) an increase in the size of the polyhedral cages, which provides guest Ba atoms more room to rattle (the 36% increase in unit cell volume should be noted), and (ii) an increase in the average mass of the framework atoms. Neither factor can explain the drastic decrease in $\kappa_{lattice}$ for $Ba_8Au_{16}P_{30}$ relative to $Ba_8Cu_{16}P_{30}$ (Table 3), as the increases in unit cell volume and average framework-atom mass for $Ba_8(Au/Cu)_{16}P_{30}$ are smaller than those for $Ba_8Ga_{16}(Ge/Sn)_{30}$. Apparently, the nanoscale interfaces formed between twinned crystallites have a considerable impact on the reduction of $\kappa_{lattice}$ for $Ba_8Au_{16}P_{30}$. The introduction of highly coherent nanoscale interfaces, which are "invisible" to the charge carriers, was shown to be an effective way to scatter heat-carrying phonons.[3] $Ba_8Au_{16}P_{30}$ offers a unique natural way to create nanoscale interfaces in the thermoelectric material. This was achieved by taking advantage of the tendency of gold atoms to relax from the "strained" tetrahedral coordination by four phosphorus atoms. This recipe can be used for the creation of new thermoelectric materials with naturally induced nanoscale interfaces.

■ CONCLUSIONS

The synthesis, crystal and electronic structures, and physical properties of the novel tetrel-free clathrate $Ba_8Au_{16}P_{30}$ have been explored. Au and P atoms segregate in the clathrate framework over different crystallographic positions, leading to a 4-fold increase of the unit cell and lowering the symmetry from cubic to orthorhombic. Crystal structure analysis and solid-state ^{31}P NMR spectroscopy indicated that one out of 15 crystallographically independent phosphorus atoms is three-coordinate. As evidenced by transmission electron microscopy, $Ba_8Au_{16}P_{30}$ exhibits the formation of a number of coherent nanoscale interfaces. These interfaces do not impede charge-carrier transport through the sample. Metal-like resistivity with holes as the main charge carriers was found for $Ba_8Au_{16}P_{30}$, as

dx.doi.org/10.1021/ja4052679 | J. Am. Chem. Soc. 2013, 135, 12313−12323

expected from the Zintl concept. However, the presence of the interfaces together with the large concentration of heavy Au atoms in the framework results in unprecendently low values of the lattice thermal conductivity for $Ba_8Au_{16}P_{30}$. We hypothesize that nanoscale interfaces are caused by the tendency of Au atoms to relax from "strained" tetrahedral coordination by P atoms. $Ba_8Au_{16}P_{30}$ is a good base for the development of efficient thermoelectric materials.

■ ASSOCIATED CONTENT

Supporting Information

Tables SI 1−4 and Figures SI 1−3. This material is available free of charge via the Internet at http://pubs.acs.org.

■ AUTHOR INFORMATION

Corresponding Author

kkovnir@ucdavis.edu

Notes

The authors declare no competing financial interest.

■ ACKNOWLEDGMENTS

This research was supported by the U.S. Department of Energy, Office of Basic Energy Sciences, Division of Materials Sciences and Engineering under Award DE-SC0008931. Use of the Advanced Photon Source at Argonne National Laboratory was supported by the U.S. Department of Energy, Office of Science, Office of Basic Energy Sciences, under Contract DE-AC02-06CH11357. We thank J. Yee for assistance with spark plasma sintering and M. Suchomel for assistance with the collection of the high-resolution XRD pattern.

■ REFERENCES

(1) Armaroli, N.; Balzani, V. *Angew. Chem., Int. Ed.* **2007**, *46*, 52−66.

(2) (a) *CRC Handbook of Thermoelectrics*; Rowe, D. M., Ed.; CRC Press: Boca Raton, FL, 1995. (b) Nolas, G. S.; Sharp, J.; Goldsmidt, H. J. *Thermoelectrics: Basic Principles and New Materials Developments*; Springer: Berlin, 2001. (c) DiSalvo, F. J. *Science* **1999**, *285*, 703−706. (d) Snyder, G. J.; Toberer, E. S. *Nat. Mater.* **2008**, *7*, 105−114. (e) Toberer, E. S.; May, A. F.; Snyder, G. J. *Chem. Mater.* **2010**, *22*, 624−634.

(3) (a) Dresselhaus, M. S.; Chen, G.; Tang, M. Y.; Yang, R.; Lee, H.; Wang, D.; Ren, Z.; Fleurial, J. P.; Gogna, P. *Adv. Mater.* **2007**, *19*, 1043−1053. (b) Sootsman, J. R.; Chung, D. Y.; Kanatzidis, M. G. *Angew. Chem., Int. Ed.* **2009**, *48*, 8616−8639. (c) Lan, Y.; Minnich, A. J.; Chen, G.; Ren, Z. F. *Adv. Funct. Mater.* **2010**, *20*, 357−376. (d) Minnich, A. J.; Dresselhaus, M. S.; Ren, Z. F.; Chen, G. *Energy Environ. Sci.* **2009**, *2*, 466−479. (e) Quarez, E.; Hsu, K.-F.; Pcionek, R.; Frangis, N.; Polychroniadis, E. K.; Kanatzidis, M. G. *J. Am. Chem. Soc.* **2005**, *127*, 9177−9190. (f) Kanatzidis, M. G. *Chem. Mater.* **2010**, *22*, 648−659.

(4) Biswas, K.; He, J.; Blum, I. D.; Wu, C.; Hogan, T. P.; Seidman, D. N.; Dravid, V. P.; Kanatzidis, M. G. *Nature* **2012**, *489*, 414−418.

(5) Mehta, R. J.; Zhang, Y.; Karthik, C.; Singh, B.; Siegel, R. W.; Borca-Tasciuc, T.; Ramanath, G. *Nat. Mater.* **2012**, *11*, 233−240.

(6) (a) Slack, G. A. In *CRC Handbook of Thermoelectrics*; Rowe, D. M., Ed.; CRC Press: Boca Raton, FL, 1995. (b) Nolas, G. S.; Slack, G. A.; Schjuman, S. B. In *Recent Trends in Thermoelectric Materials Research*; Tritt, T. M., Ed.; Academic Press: San Diego, 2001. (c) Shevelkov, A. V. *Russ. Chem. Rev.* **2008**, *77*, 1−19. (d) Beekman, M.; Nolas, G. S. *J. Mater. Chem.* **2008**, *18*, 842−851. (e) Sales, B. C. *Int. J. Appl. Ceram. Technol.* **2007**, *4*, 291−296. (f) Christensen, M.; Johnsen, S.; Iversen, B. B. *Dalton Trans.* **2010**, *39*, 978−992. (g) Paschen, S.; Godart, C.; Grin, Yu. In *Complex Metallic Alloys: Fundamentals and Applications*; Dubois, J.-M., Belin-Ferré, E., Eds.; Wiley-VCH, Weinheim, Germany, 2011.

(7) (a) Bobev, S.; Sevov, S. C. *J. Solid State Chem.* **2000**, *153*, 92−105. (b) Kovnir, K. A.; Shevelkov, A. V. *Russ. Chem. Rev.* **2004**, *73*, 923−938. (c) Shevelkov, A. V.; Kovnir, K. *Struct. Bonding (Berlin)* **2011**, *139*, 97−142.

(8) Kasper, S.; Hagenmuller, P.; Pouchard, M.; Cros, C. *Science* **1965**, *150*, 1713−1714.

(9) (a) Dünner, J.; Mewis, A. *Z. Anorg. Allg. Chem.* **1995**, *621*, 191−196. (b) Liu, Y.; Wu, L.-M.; Li, L.-H.; Du, S.-W.; Corbett, J. D.; Chen, L. *Angew. Chem., Int. Ed.* **2009**, *48*, 5305−5308. (c) Zheng, W. Z.; Wang, P.; Wu, L.-M.; Liu, Y.; Chen, L. *Inorg. Chem.* **2010**, *49*, 5890−5896. (d) Kovnir, K.; Stockert, U.; Budnyk, S.; Prots, Yu.; Baitinger, M.; Paschen, S.; Shevelkov, A. V.; Grin, Yu. *Inorg. Chem.* **2011**, *50*, 10387−10396. (e) He, H.; Zevalkink, A.; Gibbs, Z. M.; Snyder, G. J.; Bobev, S. *Chem. Mater.* **2012**, *24*, 3596−3603.

(10) Petricek, V.; Dusek, M.; Palatinus, L. *JANA2006: The Crystallographic Computing System*; Institute of Physics: Praha, Czech Republic, 2006.

(11) (a) *SMART*; Bruker AXS Inc.: Madison, WI, 2007. (a) *SAINT*; Bruker AXS Inc.: Madison, WI, 2007.

(12) Sheldrick, G. M. *TWINABS*; University of Göttingen: Göttingen, Germany, 1996.

(13) Sheldrick, G. M. *Acta Crystallogr.* **2008**, *A64*, 112−122.

(14) (a) *CrystalMaker*; CrystalMaker Software Ltd.: Begbroke, U.K., 2013. (b) Momma, K.; Izumi, F. *J. Appl. Crystallogr.* **2008**, *41*, 653−658. (c) *MacTempas*; Total Resolution LLC: Berkeley, CA, 2013. (d) *CrystalKit*; Total Resolution LLC: Berkeley, CA, 2013.

(15) Massiot, D.; Fayon, F.; Capron, M.; King, I.; Le Calve, S.; Alonso, B.; Durand, J.-O.; Bujoli, J.-O.; Gan, Z.; Hoatson, G. *Magn. Reson. Chem.* **2002**, *40*, 70−76.

(16) Fulmer, J.; Kaseman, D. C.; Dolyniuk, J.-A.; Lee, K.; Sen, S.; Kovnir, K. *Inorg. Chem.* **2013**, *52*, 7061−7067.

(17) Bilbao Crystallographic Server. http://www.cryst.ehu.es/ (accessed April 18, 2012).

(18) (a) Shatruk, M. M.; Kovnir, K. A.; Lindsjö, M.; Presniakov, I. A.; Kloo, L. A.; Shevelkov, A. V. *J. Solid State Chem.* **2001**, *161*, 233−242. (b) Carrillo-Cabrera, W.; Budnyk, S.; Prots, Yu.; Grin, Yu. *Z. Anorg. Allg. Chem.* **2004**, *630*, 2267−2276. (c) Dubois, F.; Fässler, T. F. *J. Am. Chem. Soc.* **2005**, *127*, 3264−3265. (d) Kaltzoglou, A.; Hoffmann, S. D.; Fässler, T. F. *Eur. J. Inorg. Chem.* **2007**, 4162−4167. (e) Kaltzoglou, A.; Fässler, T. F.; Christensen, M.; Johnsen, S.; Iversen, B. B.; Presniakov, I. A.; Sobolev, A. V.; Shevelkov, A. V. *J. Mater. Chem.* **2008**, *18*, 5630−5637. (f) Kaltzoglou, A.; Fässler, T. F.; Gold, C.; Scheidt, E.-W.; Scherer, W.; Kume, T.; Shimizu, H. *J. Solid State Chem.* **2009**, *182*, 2924−2929. (g) Zaikina, J. V.; Kovnir, K. A.; Sobolev, A. V.; Presniakov, I. A.; Prots, Yu.; Baitinger, M.; Schnelle, W.; Olenev, A. V.; Lebedev, O. I.; Van Tendeloo, G.; Grin, Yu.; Shevelkov, A. V. *Chem.—Eur. J.* **2007**, *13*, 5090−5099. (h) Kirsanova, M. A.; Reshetova, L. N.; Olenev, A. V.; Abakumov, A. M.; Shevelkov, A. V. *Chem.—Eur. J.* **2011**, *17*, 5719−5726. (i) Kirsanova, M. A.; Mori, T.; Maruyama, S.; Matveeva, M.; Batuk, D.; Abakumov, A. M.; Gerasimenko, A. V.; Olenev, A. V.; Grin, Yu.; Shevelkov, A. V. *Inorg. Chem.* **2013**, *52*, 577−588.

(19) Werner, P.-E.; Eriksson, L.; Westdahl, M. *J. Appl. Crystallogr.* **1985**, *18*, 367−370.

(20) Liebau, F. *Structural Chemistry of Silicates: Structure, Bonding, and Classification*; Springer: Berlin, 1985.

(21) (a) Cordier, G.; Woll, P. *J. Less-Common Met.* **1991**, *169*, 291−302. (b) Fässler, T. F.; Kronseder, C. *Z. Anorg. Allg. Chem.* **1998**, *624*, 561−568. (c) Melnychenko-Koblyuk, N.; Grytsiv, A.; Rogl, P.; Rotter, M.; Lackner, R.; Bauer, E.; Fornasari, L.; Marabelli, F.; Giester, G. *Phys. Rev. B* **2007**, *76*, No. 195124. (d) Kaltzoglou, A.; Ponou, S.; Fässler, T. F. *Eur. J. Inorg. Chem.* **2008**, 538−542. (e) Kaltzoglou, A.; Ponou, S.; Fässler, T. F. *Eur. J. Inorg. Chem.* **2008**, 4507−4510. (f) Zhang, H.; Borrmann, H.; Oeschler, N.; Candolfi, C.; Schnelle, W.; Schmidt, M.; Burkhardt, U.; Baitinger, M.; Zhao, J.-T.; Grin, Yu. *Inorg. Chem.* **2011**, *50*, 1250−1257. (g) Aydemir, U.; Candolfi, C.; Ormeci, A.; Oztan, Y.; Baitinger, M.; Oeschler, N.; Steglich, F.; Grin, Yu. *Phys. Rev. B* **2011**, *84*, No. 195137. (h) Zeiringer, I.; Chen, M.; Grytsiv, A.; Bauer, E.;

Podloucky, R.; Effenberger, H.; Rogl, P. *Acta Mater.* **2012**, *60*, 2324−2336.
(22) Möller, M. H.; Jeitschko, W. *Z. Anorg. Allg. Chem.* **1982**, *491*, 225−236.
(23) Jeitschko, W.; Möller, M. H. *Acta Crystallogr.* **1979**, *B35*, 573−579.
(24) von Schnering, H. G.; Hönle, W. *Chem. Rev.* **1988**, *88*, 243−273.
(25) Emsley, J. *The Elements*, 3rd ed.; Clarendon Press: Oxford, U.K., 1998.
(26) Chikhrii, S. I. *Russ. J. Inorg. Chem.* **1990**, *35*, 942−944.
(27) Iandelli, A. *Atti Accad. Naz. Lincei, Rend., Cl. Sci. Fis., Mat. Nat.* **1952**, *13*, 144−151.
(28) (a) Papoyan, G.; Hoffmann, R. *Angew. Chem., Int. Ed.* **2000**, *39*, 2408−2448. (b) Mizoguchi, H.; Hosono, H. *J. Am. Chem. Soc.* **2011**, *133*, 2394−2397. (c) Wang, P. L.; Kolodiazhnyi, T.; Yao, J.; Mozharivskyj, Y. *J. Am. Chem. Soc.* **2012**, *134*, 1426−1429. (d) Wang, P. L.; Kolodiazhnyi, T.; Yao, J.; Mozharivskyj, Y. *Chem. Mater.* **2013**, *25*, 699−703.
(29) *Chemistry, Structure and Bonding of Zintl Phases and Ions*; Kauzlarich, S. M., Ed.; VCH: New York, 1996.
(30) Miller, G. J.; Schmidt, M. W.; Wang, F.; You, T.-S. *Struct. Bonding (Berlin)* **2011**, *139*, 1−55.
(31) (a) Pfannenschmidt, U.; Behrends, F.; Lincke, H.; Eul, M.; Schäfer, K.; Eckert, H.; Pöttgen, R. *Dalton Trans.* **2012**, *41*, 14188−14196. (b) Bartsch, T.; Wiegand, T.; Ren, J.; Eckert, H.; Johrendt, D.; Niehaus, O.; Eul, M.; Pöttgen, R. *Inorg. Chem.* **2013**, *52*, 2094−2102.
(32) Carrillo-Cabrera, W.; Borrmann, H.; Paschen, S.; Baenitz, M.; Steglich, F.; Grin, Yu. *J. Solid State Chem.* **2005**, *178*, 715−728.
(33) (a) Nistor, L.; Van Tendeloo, G.; Amelinckx, S.; Cros, C. *Phys. Status Solidi A* **1994**, *146*, 119−132. (b) Kovnir, K. A.; Sobolev, A. V.; Presniakov, I. A.; Lebedev, O. I.; Van Tendeloo, G.; Schnelle, W.; Grin, Yu.; Shevelkov, A. V. *Inorg. Chem.* **2005**, *44*, 8786−8793. (c) Guloy, A. M.; Ramlau, R.; Tang, Z.; Schnelle, W.; Baitinger, M.; Grin, Yu. *Nature* **2006**, *443*, 320−323. (d) Kovnir, K. A.; Abramchuk, N. S.; Zaikina, J. V.; Baitinger, M.; Burkhardt, U.; Schnelle, W.; Olenev, A. V.; Lebedev, O. I.; Van Tendeloo, G.; Dikarev, E. V.; Shevelkov, A. V. *Z. Kristallogr.* **2006**, *221*, 527−532. (e) Okamoto, N. L.; Oh, M. W.; Nishii, T.; Tanaka, K.; Inui, H. *J. Appl. Phys.* **2006**, *99*, No. 033513. (f) Jung, W.; Lörincz, J.; Ramlau, R.; Borrmann, H.; Prots, Yu.; Haarmann, F.; Schnelle, W.; Burkhardt, U.; Baitinger, M.; Grin, Yu. *Angew. Chem., Int. Ed.* **2007**, *46*, 6725−6728.
(34) Avila, M. A.; Suekuni, K.; Umeo, K.; Fukuoka, H.; Yamanaka, S.; Takabatake, T. *Phys. Rev. B* **2006**, *74*, No. 125109.
(35) Bentien, A.; Christensen, M.; Bryan, J. D.; Sanchez, A.; Paschen, S.; Steglich, F.; Stucky, G. D.; Iversen, B. B. *Phys. Rev. B* **2004**, *69*, No. 045107.
(36) Sales, B. C.; Chakoumakos, B. C.; Jin, R.; Thompson, J. R.; Mandrus, D. *Phys. Rev. B* **2001**, *63*, No. 245113.
(37) Avila, M. A.; Suekuni, K.; Umeo, K.; Fukuoka, H.; Yamanaka, S.; Takabatake, T. *Appl. Phys. Lett.* **2008**, *92*, No. 041901.
(38) Suekuni, K.; Avila, M. A.; Umeo, K.; Fukuoka, H.; Yamanaka, S.; Nakagawa, T.; Takabatake, T. *Phys. Rev. B* **2008**, *77*, No. 235119.
(39) Huo, D.; Sasakawa, T.; Muro, Y.; Takabatake, T. *Appl. Phys. Lett.* **2003**, *82*, 2640−2642.
(40) Schmitt, D. C.; Haldolaarachchige, N.; Xiong, Y.; Young, D. P.; Jin, R.; Chan, J. Y. *J. Am. Chem. Soc.* **2012**, *134*, 5965−5973.
(41) Kurosaki, K.; Kosuga, A.; Muta, H.; Uno, M.; Yamanaka, S. *Appl. Phys. Lett.* **2005**, *87*, No. 061919.
(42) (a) Kovnir, K.; Shatruk, M. *Eur. J. Inorg. Chem.* **2011**, 3955−3962. (b) Mudryk, Y.; Manfrinetti, P.; Smetana, V.; Liu, J.; Fornasini, M. L.; Provino, A.; Pecharsky, V. K.; Miller, G. J.; Gschneidner, K. A., Jr. *J. Alloys Compd.* **2013**, *557*, 252−260.